ADVANCED FUNCTIONAL MATERIALS
www.afm-journal.de

Asymmetric Bond Delta-Polarization at the Interfacial Se—Ru—O Bridge for Efficient pH-Robust Water Electrolysis

*Ya Chen, Yaoda Liu, Lei Li, Thangavel Sakthive, Zhixin Guo, and Zhengfei Dai**

The rationalization of pH-robust catalysis is highly desired but challengeable for overall water electrolysis (WE). It requests a metal active site that can make an efficient adaption with both cathodic hydrogen and anodic oxygen evolution reactions (HER/OER). Herein, a $RuO_{2-x}/RuSe_2$ heterostructure electrocatalyst is profiled with interfacial Se—Ru—O bridge for the pH-robust water splitting studies. An asymmetric bond delta-polarization (Δp) is found at the interfacial Se—Ru—O bridge, including the Δp > 0 at the Ru—O part and Δp < 0 at the Ru—Se side by both experiment and calculation results. The enlarged Ru—O bond polarizability (Δp > 0) can in principle trigger the lattice oxygen mediated (LOM) pathway for OER; meanwhile, the reduced Ru—Se bond polarizability can benefit the HER due to the strengthened d-p band hybridization. Resultantly, the heterostructure can deliver ultralow overpotentials of 25/10 mV for Pt-beyond HER and 210/255 mV for OER at 10 mA cm^{-2} in acidic/alkaline media, respectively. In especial, the acidic overall WE can be stably operated for 200 h with a low cell voltage of 1.478 V at 10 mA cm^{-2}. This research clarifies the asymmetric bond polarization as the criterion for the rational design of efficient WE catalysts.

1. Introduction

Hydrogen is recognized as a preferential candidate to realize pollution-free and sustainable energy conversion protocols.[1] Among various techniques, water electrolysis (WE) promises the ecofriendly manner for hydrogen production, but it should be kinetically accelerated by efficient catalysts.[2] For the cathodic hydrogen evolution reaction (HER), Pt-group metals (PGMs) are regarded as the benchmarks due to its high electrocatalytic activity and stability.[3] Among the PGMs, Ruthenium with lower price and intense H affinitive capacity (≈65 kcal·mol^{-1}) has been deemed as an alternative substitute for Pt benchmark.[4] While from Sabatier's principle, it still necessitates the Ru-based catalysts to a moderate H affinity with near-neutral-adsorption dynamics ($\Delta G_{H^*} \approx 0$).[5] It is indicated that the introduction of non-metallic elements (NME, Se, S, etc.) can offer an effective measure to balance the hydrogen adsorption/desorption behavior for higher HER activity.[6] The bond polarization between them will lighten the strong H-Ru adsorption and induce a Ru/NME dual-site boosted HER kinetics through the d/p band center regulation.[7] Although the Ru-compounds currently achieved excellent properties for HER, the extensive WE utilization is significantly impeded by the sluggish anodic multi-step oxygen evolution reaction (OER).[8] Besides, the practical WE devices appeals for the electrocatalysts that can tolerate the pH-fluctuation for long-term operation.[9] Hence, there is a pressing need for an efficient and pH-robust Ru-based catalyst capable of accelerating HER kinetics while also exhibiting OER activity.

For the anode-side OER process, it still remains a bottleneck limitation in acidic condition due to the severe corrosion issue.[10] Currently, PGM oxides (e.g., RuO_2) have gained ever-increasing attention for their corrosion-resistive acidic OER properties.[11] While in the OER activity promotion, it is always confined by the Sabatier's adsorbate evolution mechanism (AEM) with the scaling relationship limitation.[12] The community has thus proposed an alternative lattice oxygen mediated (LOM) pathway to overpass this scaling limitation, in which the OER process can be promoted by direct $O_{Lattice}$-$^*O$ coupling.[13] But this in turn leads to an excessive oxidation of Ru^{4+} sites to acidic-soluble $Ru^{(4+\delta)+}$ species toward a deteriorated OER durability.[10a] The Ru—O bond modulation should be the fundamental in the design of stable and active RuO_2 catalysts.[14] To alleviate the $Ru^{4+} \rightarrow Ru^{(4+\delta)+}$ route, it will be feasible to introduce low-valence Ru < 4+ sites in RuO_2 to block its direct-oxidation into soluble $Ru^{(4+\delta)+}$. Meanwhile, the presence of low-valence Ru < 4+ sites will also enlarge the Ru—O bond polarizability and weaken the lattice oxygen confinement to benefit the LOM pathway.[15] But for the e^--accepting HER, a reduced Ru-bond polarizability is demanded to raise the e^--cloud overlap between the Ru and non-metal element sites for proton adsorption.[16] Hence, asymmetric bond polarization at the Ru sites is expected to actively couple the HER and OER for pH-robust water electrolysis.

Y. Chen, Y. Liu, L. Li, Z. Guo, Z. Dai
State Key Laboratory for Mechanical Behavior of Materials
Xi'an Jiaotong University
Xi'an 710049, P. R. China
E-mail: sensdai@mail.xjtu.edu.cn
T. Sakthive
Department of Chemical Engineering
Kumoh National Institute of Technology
Gyeongbuk 39177, South Korea

The ORCID identification number(s) for the author(s) of this article can be found under https://doi.org/10.1002/adfm.202406587

DOI: 10.1002/adfm.202406587

In this study, we have profiled a $RuO_{2-x}/RuSe_2$ heterostructure as an effective platform for the pH-robust WE performance and catalytic mechanism studies. The electronspun $RuO_{2-x}/RuSe_2$ nanofibers is featured with the diameter of ca. 100 nm and via-hole porous structure. It is revealed that the $RuO_{2-x}/RuSe_2$ heterostructure undertakes an asymmetric bond delta-polarization (Δp) at the formed interfacial Se—Ru—O bridge. The enlarged Ru—O bond polarizability ($\Delta p > 0$) can in principle activate the lattice oxygen mediated (LOM) pathway for the boosted OER process. Meanwhile, the decreased Ru—Se bond polarizability ($\Delta p < 0$) can benefit the HER kinetics due to the enhanced d_{Ru}-p_{Se} band hybridization. As expected, the optimized $RuO_{2-x}/RuSe_2$ heterostructure exhibits the efficient HER/OER catalytic activity and stability in both acidic and alkaline media (25/210 mV in 0.5 M H_2SO_4, 10/255 mV in 1 M KOH, at 10 mA cm^{-2}). Especially, the overall WE can be stably delivered for 200 h with ultralow operation cell voltages of 1.478 and 1.496 V to reach 10 mA cm^{-2} in 0.5 M H_2SO_4 and 1 M KOH, respectively. This work opens up the interesting possibilities for the rational design of efficient bifunctional WE electrocatalysts through bond polarization engineering.

2. Results and Discussion

2.1. Morphology, Phase, and Surface Chemical State Studies

Figure 1a depicts the synthesis process of hollow carbon wrapped $RuO_{2-x}/RuSe_2$ heterostructure ($RuO_{2-x}/RuSe_2$@CNF) by a facile electrospinning/calcination process. The detailed synthetic procedures are described in the supplementary information. Figure 1b presents the scanning electron microscope (SEM) image of the as-obtained $RuO_{2-x}/RuSe_2$@CNF with an intact fibrous hollow structure. The Brunauer–Emmett–Teller (BET) surface area is determined to be 71.40 m^2 g^{-1} (Figure S1, Supporting Information).[17] Such a conductive porous skeleton would merit the active site exposure, electron transport, and bubble release in the electrochemical catalysis.[18] The similar morphological features of $RuO_2/RuSe_2$@CNF fabricated with different Se source amount are also depicted in Figure S2 (Supporting Information). The microstructures of the fibrous $RuO_{2-x}/RuSe_2$@CNF were characterized by transmission electron microscopy (TEM, Figure 1c–e; Figure S3, Supporting Information). The well-defined $RuO_{2-x}/RuSe_2$ nanoparticles (NPs) in carbon matrix can not only prevent their detachment and self-aggregation but also ensure the electronic conductivity.[19] The average NP size was determined as ca. ≈25.4 nm (Figure S4). In the high-resolution TEM (HRTEM, Figure 1d; Figure S5, Supporting Information) images, the *d*-spacing of 0.320 and 0.299 nm can be respectively indexed as the (110) plane of tetragonal RuO_2 and (200) plane of cubic $RuSe_2$.[20] Corresponding elemental mapping image further confirms the uniform distribution of Ru, Se, C, O, and N elements throughout the fibrous heterostructure (Figure 1e). The Ru content in the $RuO_{2-x}/RuSe_2$@CNF catalyst was determined to be ≈8.2 wt% (Table S1, Supporting Information) by inductively coupled plasma-mass spectrometry (ICP-MS) test.

X-ray diffraction (XRD) was applied to examine the phase information of the $RuO_2/RuSe_2$@CNF heterostructure and other control samples (Figure 1f; Figure S6, Supporting Information). For $RuO_{2-x}/RuSe_2$@CNF, the typical XRD peaks located at 27.96°/35.08°/40.21°/54.27° correspond to the (110)/(101)/(200)/(211) planes of RuO_2 (JCPDS No. 43–1027);[21] and the peaks at 30.06°, 33.68°, 37.10°, 43.05°, 50.95°, 55.74°, 58.08° can be assigned to the (200), (210), (211), (220), (311), (230), and (321) planes of $RuSe_2$ (JCPDS No. 03–1198).[6c,22] In addition, the structures of RuO_{2-x}@CNF and $RuSe_2$@CNF were also characterized for reference in Figures S7 and S8 (Supporting Information). All the above results suggest the successful formation of $RuO_{2-x}/RuSe_2$ hetero-interfaces in the porous CNF matrix. The surface states were further checked by Raman, electron paramagnetic resonance (EPR), and X-ray photoelectron spectroscopy (XPS). Figure 1g displays the Raman spectra of $RuSe_2$@CNF, $RuO_{2-x}/RuSe_2$@CNF, and RuO_{2-x}@CNF. For the RuO_{2-x}@CNF sample, three distinctive peaks at 515.3, 631.1, and 693.5 cm^{-1} can be ascribed to the E_g, A_{1g}, and B_{2g} vibration modes of RuO_2, respectively.[20] Compared to RuO_{2-x}@CNF, the RuO_2-B_{2g} peak intensity of $RuO_{2-x}/RuSe_2$@CNF obviously declined due to the surface selenization. With the oxygen-extracted selenization, more oxygen vacancies can be found in the $RuO_{2-x}/RuSe_2$@CNF, as reflected by the slightly increased EPR signal at g = 2.005 (Figure 1h).[11a] The Fourier transform infrared spectroscopy (FT-IR) in Figure S9 (Supporting Information) shows that the $RuO_{2-x}/RuSe_2$@CNF possesses a higher O—H vibration intensity than RuO_{2-x}@CNF and $RuSe_2$@CNF, indicating better hydrophilicity.[23] Besides, the $RuO_{2-x}/RuSe_2$@CNF shows the smallest contract angle (CA, 11.5°) in comparison with RuO_{2-x}@CNF and $RuSe_2$@CNF (Figure S10, Supporting Information), implying the higher hydrophilicity and more efficient water adsorption.[24]

The chemical states of these samples were further investigated by XPS in Figure 1i–k and Figure S11 (Supporting Information). As depicted in Figure 1i, the high-resolution Ru 3p spectrum of RuO_{2-x}@CNF exhibits two typical characteristic peaks centered at 463.36 and 485.60 eV, attributed to the Ru $3p_{3/2}$ and Ru $3p_{1/2}$ of Ru—O bond in RuO_2, respectively.[25] After selenization treatment, two additional deconvoluted peaks at 461.60 and 483.87 eV can be assigned to the Ru $3p_{3/2}$ and Ru $3p_{1/2}$ of Ru—Se bond in $RuSe_2$, manifesting the formation of the Se—Ru—O link in the heterostructure.[6c] Besides, the Se 3d XPS spectrum for $RuO_{2-x}/RuSe_2$@CNF (Figure 1j) splits into three characteristic peaks, including Se $3d_{5/2}$ (55.37 eV), Se $3d_{3/2}$ (56.21 eV), and SeO_x (59.01 eV).[26] Compared with $RuSe_2$@CNF, the Se 3d binding energy of $RuO_{2-x}/RuSe_2$@CNF exhibits an obvious positive-shift about 0.8 eV, indicating the $RuSe_2 \rightarrow RuO_{2-x}$ electron transfer direction in the heterostructure. This electron transfer manner can be also reflected by the O1s XPS results in Figure 1k, where the $RuO_{2-x}/RuSe_2$@CNF peaks are slightly red-shifted relative to RuO_{2-x}@CNF. Such a selenide-to-oxide interfacial electron transfer behavior can be also understood by their distinctive Se/O electronegativity difference (Figure S12, Supporting Information).[27] From the O 1s XPS data, the heterostructure shows the higher contents of oxygen vacancies (530.06 eV) and surface hydroxyl group (531.93 eV),[28] in accordance with the EPR and FT-IR/CA results. The strong interfacial interactions will tune the whole electronic structure of the heterostructure, and the enhanced hydrophilicity can benefit the water adsorption.

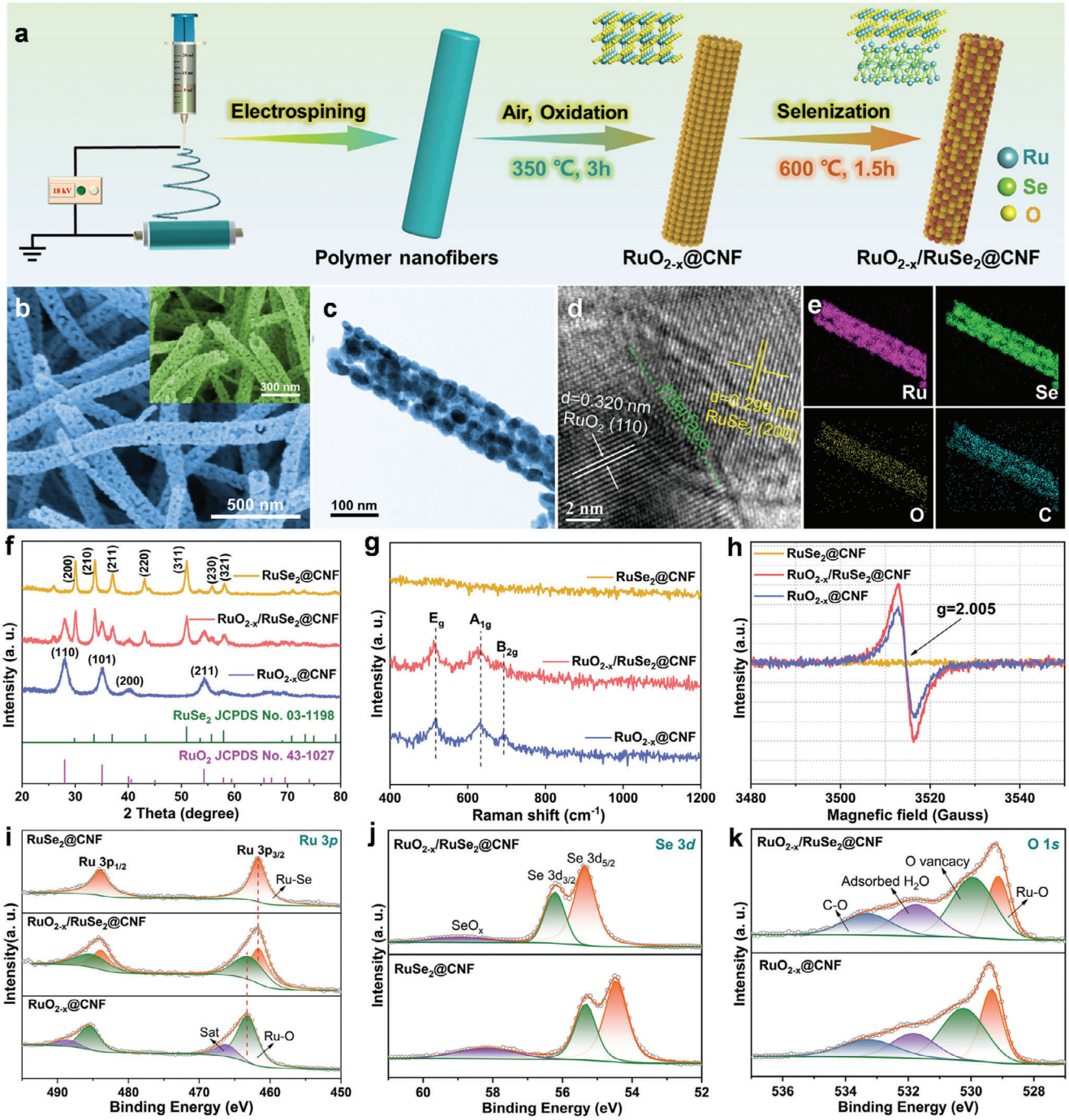

Figure 1. Synthesis scheme and structural characterizations. a) Schematic diagram for the synthesis of $RuO_{2-x}/RuSe_2$@CNF. b) SEM image of $RuO_{2-x}/RuSe_2$@CNF (inset: cross-section SEM image). c) TEM image, d) HR-TEM image, and e) elemental mapping of $RuO_{2-x}/RuSe_2$@CNF. f) XRD pattern, g) Raman spectra, and h) EPR spectra of RuO_{2-x}@CNF, $RuO_{2-x}/RuSe_2$@CNF, and $RuSe_2$@CNF. i) Ru 3p, j) Se 3d, and k) O 1s XPS spectra of RuO_{2-x}@CNF, $RuO_{2-x}/RuSe_2$@CNF, and $RuSe_2$@CNF.

2.2. Coordination Environment and Bond Polarization

X-ray absorption near-edge structure (XANES) and Fourier-transformed EXAFS (FT-EXAFS) were further conducted to investigate the Ru chemical environment of these materials. As presented in **Figure** 2a, the white-line of Ru K-edge XANES for $RuO_{2-x}/RuSe_2$@CNF is located between Ru foil and RuO_2. It reveals that the average Ru oxidation state in the heterostructure is between Ru^0 and Ru^{4+}.[29] The fitted Ru valence state in the $RuO_{2-x}/RuSe_2$@CNF is of ca. +2.28 between the RuO_{2-x}@CNF (+3.32) and $RuSe_2$@CNF (+0.85), as shown in Figure 2b. This also suggests the RuO_{2-x} and $RuSe_2$ behave the electronic

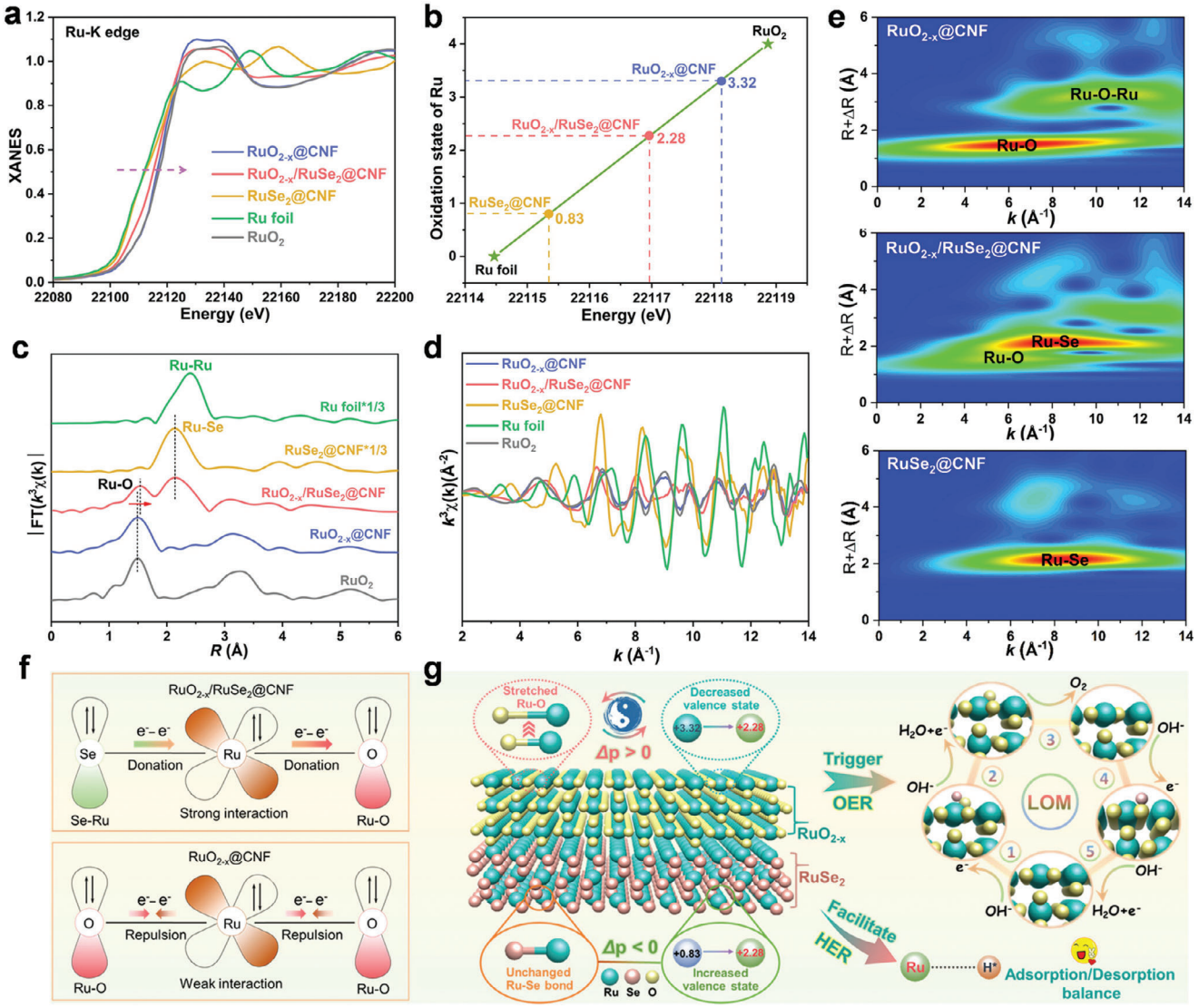

Figure 2. EXAFS spectra and analyses. a) Ru K-edge XANES, b) Average oxidation states of Ru from XANES spectra, c) Ru K-edge FT-EXAFS, d) Ru K-edge EXAFS oscillation function, and e) Wavelet transform for k^3-weighted EXAFS signal of RuO_{2-x}@CNF, RuO_{2-x}/$RuSe_2$@CNF, and $RuSe_2$@CNF. f) The effects of Ru—O bond length/valence on bond polarizability. g) The delta-bond polarizability (Δp) at Se—Ru—O interfacial bridge and its effect on OER/HER catalysis.

acceptor and donor in the heterostructure, respectively. Figure 2c presents the corresponding FT-EXAFS spectra of the different samples. For the RuO_{2-x}/$RuSe_2$@CNF, two scattering peaks at 1.54 and 2.14 Å are ascribable to the Ru—O and Ru—Se coordination.[6a,10a] Relative to the RuO_{2-x}@CNF, the Ru—O bond is slightly stretched in RuO_{2-x}/$RuSe_2$@CNF heterostructure (1.48 → 1.54 Å), illustrating a stretched Ru—O bond after RuO_{2-x}-$RuSe_2$ incorporation. The Ru K-edge oscillation curves in Figure 2d also indicate the different local atomic arrangements and structural distortion of the Ru sites in the heterostructure. which is vividly reflected by the wavelet transform EXAFS (WT-EXAFS) analyses in Figure 2e and Figure S13 (Supporting Information). Based on the above XPS and XAFS results, the strong electronic interactions between RuO_{2-x} and $RuSe_2$ is configured via the asymmetric Se—Ru—O interfacial bridge, accelerating the charge transport from Se sites to Ru-bound O (Figure 2f).[28a]

Moreover, the bond configuration change will impact the interactions between the catalysts and adsorbates to regulate the electrocatalytic properties. According to Coulomb's law ($F \propto Qq/r^2$), the bond strength (F) is highly related to atomic valence charge (Q, q) and bond length and bond length r (Figure S14, Supporting Information).[30] Generally, the bond-length stretch and valence decrease will result in a weaker bond strength, and thus bring an increased bond polarizability (Δp > 0).[15] Here in the Se—Ru—O bridge, the Ru—O half edge undergoes the bond stretching and valence decrease (+3.32 → +2.28) relative to the RuO_{2-x}, giving rise to an increased bond polarizability (Δp > 0); while for Ru—Se half edge in the bridge, it concludes a decreased bond polarizability (Δp < 0) against the $RuSe_2$. Therefore, a Janus

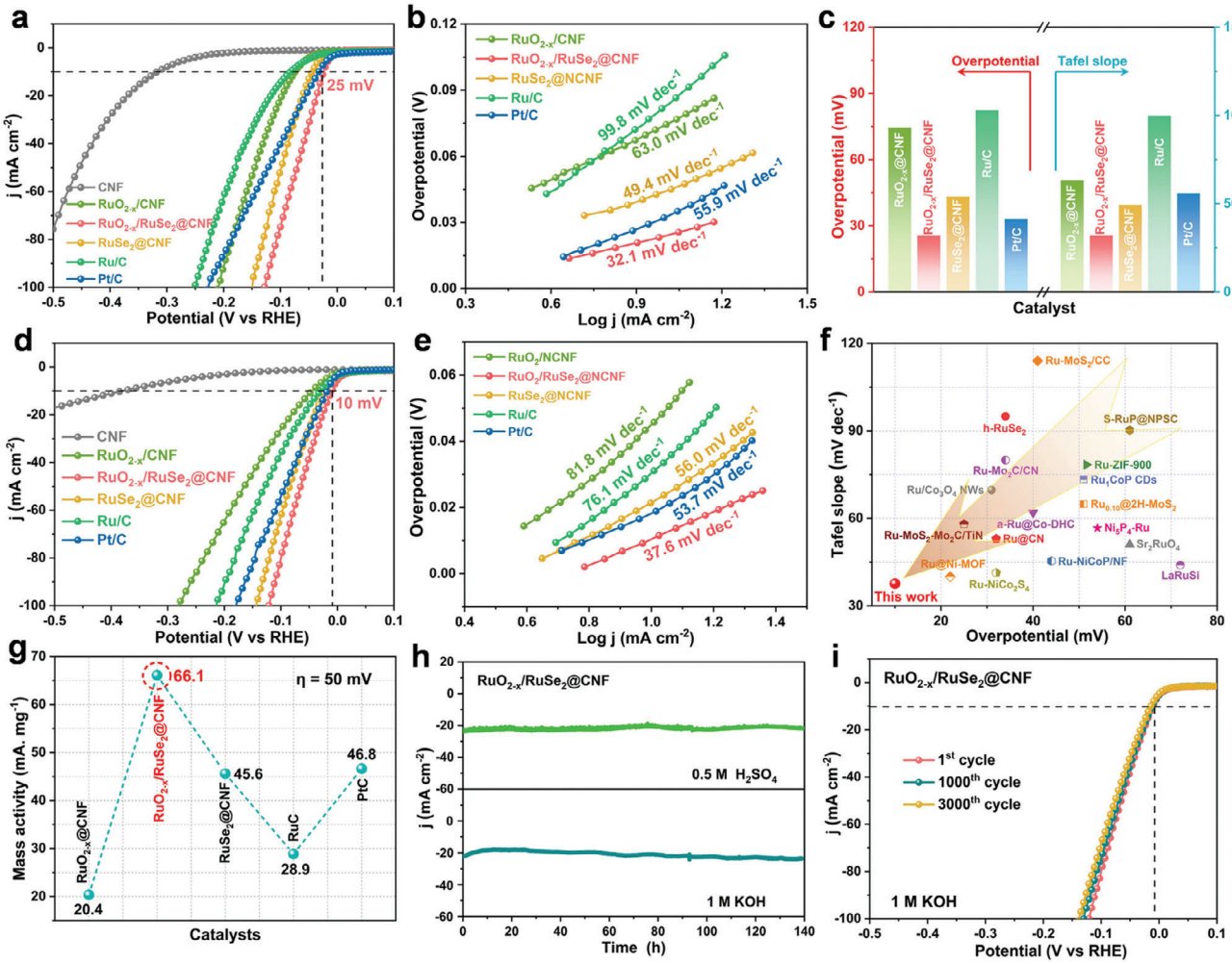

Figure 3. Electrocatalytic HER performances. a) LSV curves, b) Tafel slopes, and c) histogram of η_{10}-Tafel slope values of different samples in 0.5 M H_2SO_4. d) LSV curves, e) Tafel plots, and f) of the HER performance comparison of $RuO_{2-x}/RuSe_2$@CNF with reported catalysts in 1 M KOH. g) Mass activities of different catalysts. h) i-t curves of $RuO_{2-x}/RuSe_2$@CNF for HER in acidic and alkaline electrolytes. i) HER LSV curves for $RuO_{2-x}/RuSe_2$@CNF after 1000th and 3000th cycles in 1 M KOH.

asymmetric bond polarization occurs at the Se—Ru—O bridge in the heterostructure (Figure 2g), which might merit the bifunctional water splitting process as follows: 1) for the Ru—O bond side with $\Delta p > 0$, a higher bond polarizability can alleviate the lattice oxygen confinement to trigger the preferable LOM pathway and break the OER scaling-relationship limitation; 2) for the Ru-Se bond side with $\Delta p < 0$, the intensified Ru—Se bond strengthens the d-p band hybridization to balance the H^* adsorption/desorption on the catalyst surface to benefit the HER kinetics.[15]

2.3. Electrocatalytic Properties for Water Splitting

The HER behaviors of different catalysts were studied in both the acidic and alkaline electrolytes by a standard three-electrode system, as shown in **Figure 3**.[31] The $RuO_{2-x}/RuSe_2$@CNF material is found with superior HER activity and kinetics with a low overpotential (η_{10}) of 25 mV at 10 mA cm^{-2} (Figure 3a) and a small Tafel slope of 32.1 mV dec^{-1} (Figure 3b) in 0.5 M H_2SO_4. By contrast (Figure 3c), other control catalysts and even the Pt/C benchmark all show higher η_{10} and hysteretic dynamics, such as RuO_{2-x}@CNF (76.2 mV, 63 mV dec^{-1}), $RuSe_2$@CNF (44.8 mV, 49.4 mV dec^{-1}), commercial Ru/C (84.1 mV, 99.8 mV dec^{-1}), and Pt/C (33.4 mV, 55.9 mV dec^{-1}). As compared with other precious metals catalysts, the $RuO_{2-x}/RuSe_2$@CNF material also shows an outperformed acidic HER properties (Table S2, Supporting Information). The electrochemical active surface area (ECSA) of different catalysts are also investigated in Figure S15 (Supporting Information), demonstrating the higher intrinsic HER activity of $RuO_{2-x}/RuSe_2$@CNF.[5] Besides, electrochemical impedance spectrometry (EIS) measurements indicate the boosted charge transport in the $RuO_{2-x}/RuSe_2$@CNF (Figure S16, Supporting Information).[32]

Further, the HER activity of each catalyst was also evaluated in 1 M KOH electrolyte. It is found that the $RuO_{2-x}/RuSe_2$@CNF catalyst delivers a Pt-beyond η_{10} overpotential of 10 mV and low Tafel slope of 37.6 mV dec^{-1} in 1 M KOH (Figure 3d,e). Such an

alkaline HER performance is far superior to Ru/C, Pt/C (19.1 mV, 53.7 mV dec^{-1}), and other controls (Figure S17, Supporting Information) as well as the state-of-the-art Ru-based HER catalysts (Figure 3f; Table S3, Supporting Information). The ECSA and EIS results further confirm that the $RuO_{2-x}/RuSe_2$@CNF processes the optimized intrinsic catalytic activity and electron-transfer characteristics among all the catalysts in alkaline HER (Figures S18 and S19, Supporting Information). In addition, the mass activities of $RuO_{2-x}/RuSe_2$@CNF in alkaline (Figure 3g) and acidic (Figure S20, Supporting Information) media were also calculated. The $RuO_{2-x}/RuSe_2$@CNF catalyst presents Pt-beyond HER mass activities in both acidic and alkaline media. The HER stability of the $RuO_{2-x}/RuSe_2$@CNF were further explored through i-t tests, as shown in Figure 3h. It clearly displays that the HER rate activity (20 mA cm^{-2}) can be maintained well without significant attenuation for 140 h in both 0.5 M H_2SO_4 and 1 M KOH. Figure S21 (Supporting Information) further shows the stable HER catalytic performance of $RuO_{2-x}/RuSe_2$@CNF under a higher current density of 100 mA cm^{-2}. The post-mortem SEM, TEM, XRD, and XPS examinations indicate the retention of $RuO_{2-x}/RuSe_2$@CNF structure under acidic/alkaline HER conditions (Figures S22–S24, Supporting Information). The pH-robust HER stability of $RuO_{2-x}/RuSe_2$@CNF can be also reflected by the cycling tests in 1 M KOH (Figure 3i) and 0.5 M H_2SO_4 (Figure S25, Supporting Information), where the currents after 3000 cycles show negligible decays. The promoted HER property can be understood by the decreased Ru—Se bond polarizability at the Se—Ru—O bridge with more balanced the H^* adsorption/desorption.

The OER performance of each catalysts was also evaluated in both acidic and alkaline media. As presented in **Figure 4**a,b, the $RuO_{2-x}/RuSe_2$@CNF catalyst delivers an ultralow η_{10} overpotential of 210 mV with fast kinetics (43.3 mV dec^{-1}) in 0.5 M H_2SO_4. As compared in Figure S26a (Supporting Information), the acidic OER performance of $RuO_{2-x}/RuSe_2$@CNF is much superior to RuO_{2-x}@CNF (245 mV, 65.6 mV dec^{-1}), $RuSe_2$@CNF (400 mV, 510.8 mV dec^{-1}), and commercial IrO_2 (270 mV, 83.8 mV dec^{-1}). Importantly, the $RuO_{2-x}/RuSe_2$@CNF exceeds most reported Ru-based acidic OER electrocatalysts in terms of η_{10} and Tafel slopes (Figure 4c; Table S4, Supporting Information). Figures S26b and S27 (Supporting Information) present the alkaline OER properties of different catalysts, where the heterostructure catalyst still displays the better alkaline OER performances (255 mV, 52.5 mV dec^{-1}) than other control catalysts and even the commercial benchmarks. The ECSA results in Figure S28 (Supporting Information) suggest that the heterostructure catalyst is endowed with a higher intrinsic alkaline OER activity. Overall, the $RuO_{2-x}/RuSe_2$@CNF catalyst has presented the optimal OER activities in both acidic and alkaline conditions (Figure S29, Supporting Information).

As for the OER durability, the $RuO_{2-x}/RuSe_2$@CNF can stably maintain the current density for 140 h and 3000 times cycling without obvious decays in both acidic (Figure 4d,e) and alkaline (Figure S30, Supporting Information) electrolytes. On the contrary, the RuO_{2-x}@CNF and commercial RuO_2 catalysts show the sharply dropped current behaviors in acidic OER processes (Figure 4d). The enhanced acidic OER stability was further illustrated by inductively coupled plasma optical emission spectrometer (ICP-OES, Figure 4f).[10a,33] The dissolved Ru amount in $RuO_{2-x}/RuSe_2$@CNF is only 1/10 of the RuO_{2-x}@CNF during the acidic OER, indicating the hindered corrosion of RuO_{2-x} after $RuSe_2$ confinement. Moreover, the post-OER TEM characterizations have demonstrated the well-persisted morphology and microstructure of the $RuO_{2-x}/RuSe_2$@CNF (Figure 4e inset; Figures S31 and S32, Supporting Information). XRD and XPS were employed to check the $RuO_{2-x}/RuSe_2$@CNF after OER test. The attenuated Ru-Se content during the OER may be attributed to the anodic oxidation and the dissolution of Se element (Figures S33 and S34, Supporting Information). This also manifests the catalytic role of Ru—O content and the protective effect of Ru—Se content for OER in the heterostructure system. In addition, we have also checked the effect of selenization degree (RuO_2/Se source ratio) on the HER/OER performances in both acidic and alkaline media (Figure S35, Supporting Information). It is suggested that a moderate selenization can make a fit between the protective and catalytic effects for the OER promotion.

Encouraged by the pH-robust HER/OER properties, the $RuO_{2-x}/RuSe_2$@CNF catalyst was further examined in symmetric overall water splitting (OWS) under acidic and alkaline media (Figure 4g–i). The $RuO_{2-x}/RuSe_2$@CNF||$RuO_{2-x}/RuSe_2$@CNF couple shows the much superior OWS performances to those commercial Pt/C||RuO_2 and Pt/C||IrO_2 pairs. It just requires ultralow cell voltages of 1.496 V (Figure 4g) and 1.478 V (Figure 4h) at 10 mA cm^{-2} to deliver the OWS in 1 M KOH and 0.5 M H_2SO_4, respectively. A solar-powered (1.48 V) OWS device was also assembled to demonstrate the effectiveness in the sustainable H_2 production (Figure 4h inset). In both alkaline and acidic electrolytes, the $RuO_{2-x}/RuSe_2$@CNF electrode can deliver a high OWS activity with a negligible attenuation rate for 200 h at 20 mA cm^{-2} (Figure 4i). It is worth noting that the $RuO_{2-x}/RuSe_2$@CNF material is among the best list of noble-metal-based OWS electrocatalysts (Figure 4j; Table S5, Supporting Information). Figure S36 (Supporting Information) presents the Faradaic efficiency (FE) of over 98.8% for the $RuO_{2-x}/RuSe_2$@CNF electrodes toward highly efficient OWS.[34]

2.4. Enhanced Mechanism Analyses

Density functional theory (DFT) calculations were employed to gain an insight into the promoted catalytic properties of the $RuO_{2-x}/RuSe_2$ heterostructure. **Figure 5**a shows the heterostructure model, and the counterpart models of RuO_{2-x} and $RuSe_2$ are presented in Figures S37 and S38 (Supporting Information). At the $RuO_{2-x}/RuSe_2$ interface, it is suggested that the electron transfers from $RuSe_2$ to RuO_{2-x} by the difference charge density simulations (Figure S39, Supporting Information). The electron localization function (ELF) map in Figure 5b further confirms the presence of strong electron coupling at the interface through the asymmetric Se—Ru—O configuration. Such a charge transport pathway was also validated by the result of their work function difference (Figure 5c). Given that water adsorption is a prerequisite step for water splitting, we further calculated the H_2O adsorption energy (ΔE_{H2O}) on RuO_{2-x}, $RuO_{2-x}/RuSe_2$, and $RuSe_2$ systems. The $RuO_{2-x}/RuSe_2$ exhibits higher ΔE_{H2O} (−1.149 eV) than the RuO_{2-x} (−0.564 eV) and $RuSe_2$ (−0.729 eV), presenting a more hydrophilic surface to benefit subsequent HER/OER catalytic steps (Figure 5d; Table S6, Supporting Information). For

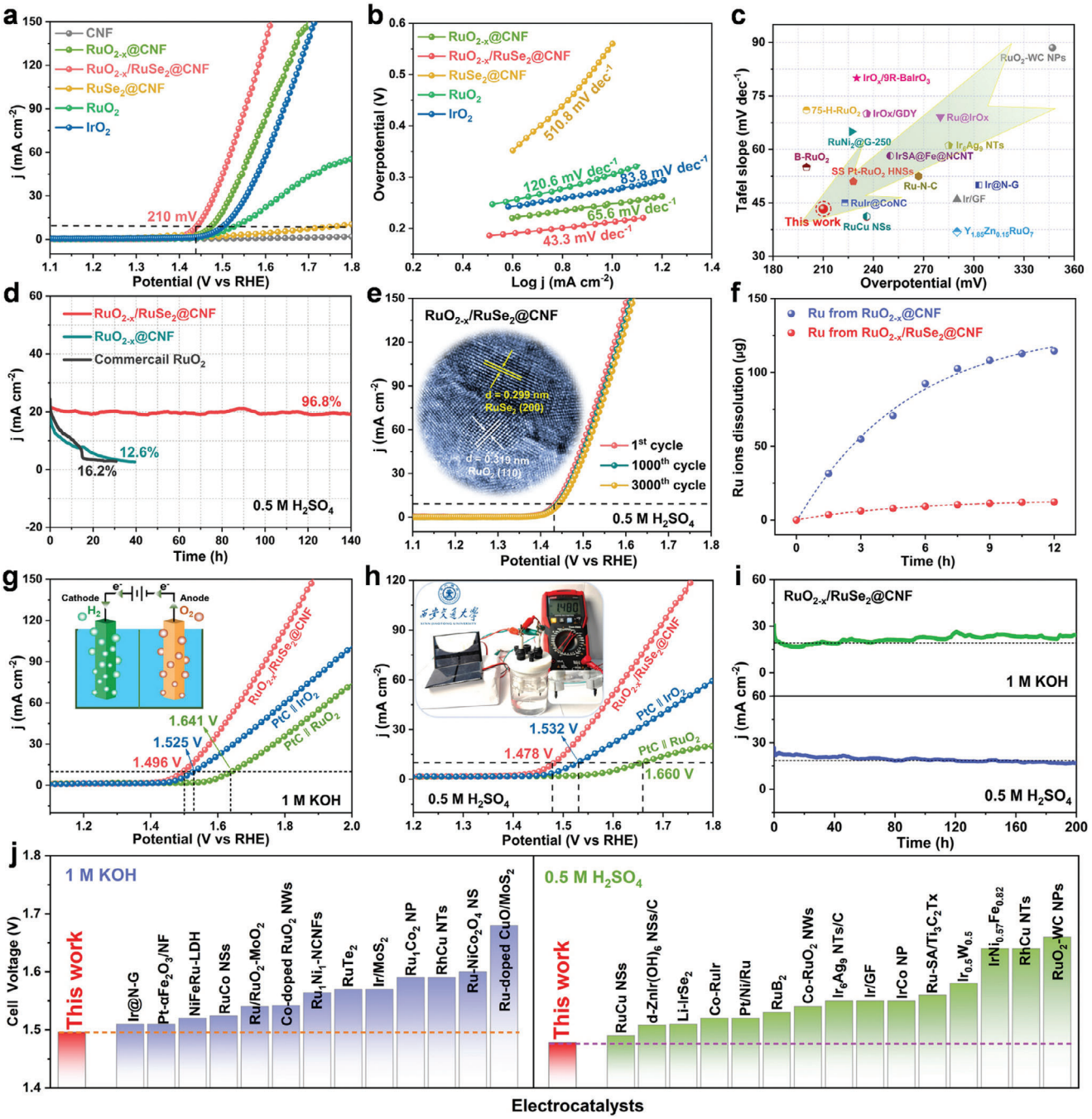

Figure 4. OER and OWS performances. a) OER polarization curves, b) Tafel slopes, and c) OER performance comparison of $RuO_{2-x}/RuSe_2$@CNF with other catalysts in 0.5 M H_2SO_4. d) I-t curves of $RuO_{2-x}/RuSe_2$@CNF, RuO_{2-x}@CNF and commercial RuO_2 at 20 mA cm^{-2} in 0.5 M H_2SO_4. e) OER LSV curves for $RuO_{2-x}/RuSe_2$@CNF after 1000th and 3000th cycles in 0.5 M H_2SO_4, inset is the post-mortem HRTEM image. f) Dissolved Ru amount during OER in 0.5 M H_2SO_4 by ICP-OES for the $RuO_{2-x}/RuSe_2$@CNF and RuO_{2-x}@CNF. OWS polarization curves of $RuO_{2-x}/RuSe_2$@CNF and controls in g) 0.5 M H_2SO_4 and h) 1 M KOH. i) I-t tests of $RuO_{2-x}/RuSe_2$@CNF||$RuO_{2-x}/RuSe_2$@CNF at 10 mA cm^{-2} in acidic and alkaline electrolytes for 200 h. j) Performance comparison of $RuO_{2-x}/RuSe_2$@ CNF with recently excellent catalysts for OWS in acidic and alkaline electrolytes, respectively.

the subsequent H_2O dissociation process, the $RuO_{2-x}/RuSe_2$ displayed the lowest H_2O dissociation energy (0.36 eV), suggesting the facilitated H_2O dissociation and H^* intermediates formation behavior (Figure S40, Supporting Information). As for HER, the hydrogen adsorption free energy (ΔG_{H^*}) was investigated for RuO_{2-x}, $RuO_{2-x}/RuSe_2$, and $RuSe_2$ catalysts.[35] From the step energy diagrams in Figure 5e, the $Ru_{@Ru\text{-}Se}$ site in the heterostructure, as the HER active center, displays the more neutral ΔG_{H^*} value (−0.053 eV) than those of Ru site in RuO_{2-x} and the Ru/Se sites in $RuSe_2$. Corresponding atomic adsorption states and

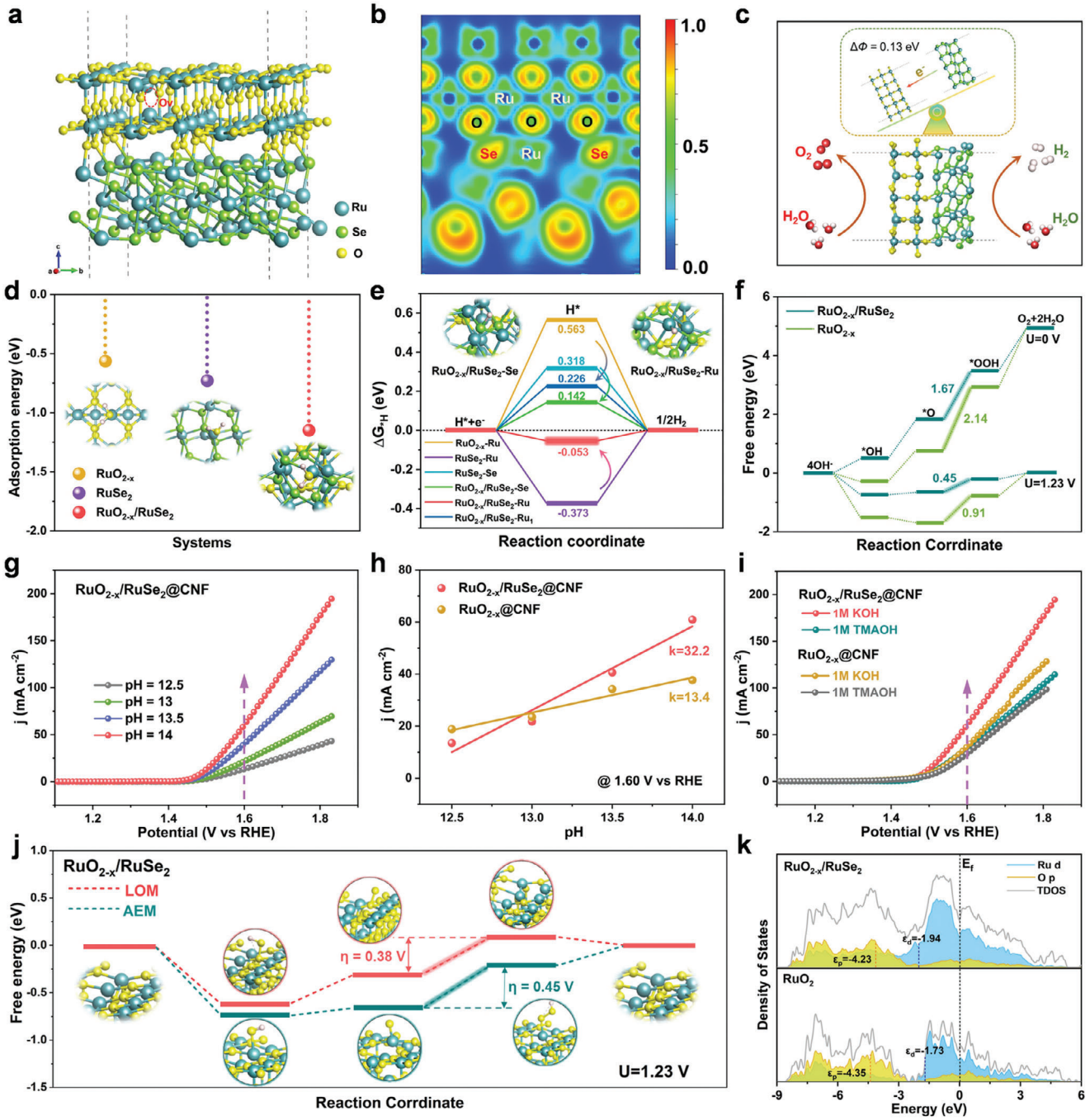

Figure 5. Catalytic enhancement mechanism analyses. a) Structure model and b) electron localization function of $RuO_{2-x}/RuSe_2$ heterostructure. c) Work function diagram between RuO_{2-x} and $RuSe_2$. d) ΔE_{H2O} on the RuO_{2-x}, $RuO_{2-x}/RuSe_2$, and $RuSe_2$ surface. e) Energy barriers for HER at different sites. f) OER free energy diagrams for $RuO_{2-x}/RuSe_2$, and RuO_{2-x}. g) OER LSV curves of $RuO_{2-x}/RuSe_2$@CNF in electrolytes with different pH values. h) Current densities of $RuO_{2-x}/RuSe_2$@CNF and $RuO_{2-x}/RuSe_2$@CNF at 1.60 V versus RHE against the pH values. i) LSV curves of $RuO_{2-x}/RuSe_2$@CNF and $RuO_{2-x}/RuSe_2$@CNF in 1 M KOH and 1 M TMAOH. j) OER energy barriers via AEM and LOM pathways on $RuO_{2-x}/RuSe_2$. k) The PDOSs projected on the O-p and Ru-d orbits for $RuO_{2-x}/RuSe_2$ and RuO_{2-x}.

calculated energy value data are presented in Figures S41 and S42 and Table S7 (Supporting Information). Such a neutral ΔG_{H^*} in the heterostructure is responsive for balancing the hydrogen ads-/de-sorption behaviors toward boosted HER performance.

Moreover, the OER pathway was investigated to decipher the OER catalytic enhancement mechanism. First of all, the conventional adsorbate evolution mechanism (AEM) was applied to discern the catalytic activity difference of $RuO_{2-x}/RuSe_2$ and RuO_{2-x} (Figure 5f; Figure S43a, Supporting Information). The

adsorption sites of the intermediates (*OH, *O, and *OOH) on each system are shown in Figures S44–S47 (Supporting Information), and Table S8 (Supporting Information) listed the corresponding calculated theoretical overpotential (η) values. It is revealed that both the rate-determining steps (RDS) of RuO_{2-x} and $RuO_{2-x}/RuSe_2$ are the evolution from *O to *OOH ($^*O \rightarrow {}^*OOH$ step) intermediates (Figure 5f). The $RuO_{2-x}/RuSe_2$ undergoes more balanced RDS energy barriers (1.67 eV@0 V and 0.45 eV@1.23 V) than that of RuO_{2-x} (2.14 eV@0 V and 0.91 eV@1.23 V), thereby strengthening the OER activity. Moreover, the $RuSe_2$ side of $RuO_{2-x}/RuSe_2$ heterostructure was also investigated, and the OER theoretical activities of the Ru/Se sites (RDS: 2.30/2.56 eV@0 V) are both inferior to the Ru site at RuO_2 side (Figures S48 and S49, Supporting Information).

In regard of the high Ru—O bond polarizability ($\Delta p > 0$), the LOM pathway would be the underlying OER manner for the $RuO_{2-x}/RuSe_2$ material.[24] Since the LOM pathway features the strong nonconcerted proton–electron coupling,[13c,36] the pH-dependent OER activities were investigated for the $RuO_{2-x}/RuSe_2$@CNF and RuO_{2-x}@CNF in Figure 5g and Figure S50 (Supporting Information). With the pH value increase from 12.5 to 14, the $RuO_{2-x}/RuSe_2$@CNF exhibits a higher *j*-pH sensitivity (Figure 5h) than RuO_{2-x}@CNF, indicating a boosted OER deprotonation process toward the LOM pathway.[18,37] To verify the proposed LOM route, the tetramethylammonium cation (TMA^+)-poisoning experiments were conducted during the OER (Figure 5i), because the TMA^+ can bind strongly with the O_2^{2-}/O^{2-} species and hamper the OER-LOM pathway.[13a,38] It is observed that the OER activity of $RuO_{2-x}/RuSe_2$@CNF declined significantly in 1 M TMAOH than that in 1 M KOH. This confirms that the LOM mode is an energetically favorable pathway for the bond-polarized $RuO_{2-x}/RuSe_2$@CNF. The free energy diagram of the multistep OER process via AEM and LOM are studied and presented in Figure 5j. The theoretical overpotential (η) of the LOM route (0.38 V) is lower than that of the AEM route (0.45 V) on the $RuO_{2-x}/RuSe_2$ heterostructure. The PDOSs of Ru_{4d} and O_{2p} orbits were plotted to further rationalize the promoted OER catalytic activity (Figure 5k). The $RuO_{2-x}/RuSe_2$ heterostructure shows the narrower d-p band center distance (4.23–1.94 = 2.29 eV) than that of RuO_{2-x} (4.35–1.73 = 2.62 eV). Such an enhanced d-p band proximity is conductive to the more balanced intermediates (*OH, *O, etc.) adsorptions and charge transport for the boosted OER process.[26]

3. Conclusion

In summary, we have profiled and fabricated a $RuO_{2-x}/RuSe_2$@CNF heterostructure by a facile electrospinning/selenization process for the efficient and pH-robust WE catalysis. The electronspun $RuO_{2-x}/RuSe_2$ nanofibers is featured with the via-hole porous structure to benefit the electrolyte accessibility. As for HER, the optimized $RuO_{2-x}/RuSe_2$ heterostructure exhibits the Pt-beyond properties with ultralow η_{10} of 10 mV in 1 M KOH and 25 mV in 0.5 M H_2SO_4. With respect to OER, the heterostructure can present the competitive performances with low η_{10} of 210 and 255 mV in acidic and alkaline electrolytes, respectively. Furthermore, the overall WE device can be stably delivered for 200 h with ultralow η_{10} cell voltages of 1.478 (acidic) and 1.496 V (alkaline), respectively. It is revealed that the $RuO_{2-x}/RuSe_2$ heterostructure features an asymmetric bond delta-polarization at the formed interfacial Se—Ru—O bridge: i) the Ru—O bond of $\Delta p > 0$ triggers the LOM pathway for OER and ii) Ru—Se bond of $\Delta p < 0$ benefits the HER kinetics by the enhanced d_{Ru}-p_{Se} band hybridization. This study carries the valuable fundamental to rationalize the pH-robust overall water splitting electrocatalysts through the interface bond modulations.

Supporting Information

Supporting Information is available from the Wiley Online Library or from the author.

Acknowledgements

This work was jointly supported by the National Natural Science Foundation of China (Grant Nos. 52371236) and the Distinguished Young Foundation of Shaanxi Province (Nos. 2024JC-JCQN-09). This research used the resources of the HPCC platform in Xi'an Jiaotong University. The authors thank Miss Liu at Instrument Analysis Center of Xi'an Jiaotong University for her assistance with XPS analysis.

Conflict of Interest

The authors declare no conflict of interest

Data Availability Statements

The data that support the findings of this study are available from the corresponding author upon reasonable request.

Keywords

asymmetric bond-delta polarization, interfacial Se—Ru—O bridge, overall water splitting, pH-robust electrocatalysis, ruthenium oxide

Received: April 18, 2024
Revised: May 25, 2024
Published online:

[1] a) B. Zhang, J. Wang, G. Liu, C. M. Weiss, D. Liu, Y. Chen, L. Xia, P. Zhou, M. Gao, Y. Liu, W. Sun, *Nat. Catal.* **2024**, *7*, 441; b) R. Detchon, R. Van Leeuwen, *Nature* **2014**, *508*, 309; c) Y. Chen, Y. Liu, W. Zhai, H. Liu, T. Sakthivel, S. Guo, Z. Dai, *Adv. Energy Mater.* **2024**, *14*, 2400059; d) X. He, P. Du, G. Yu, R. Wang, Y. Long, B. Deng, C. Yang, W. Zhao, Z. Zhang, K. Huang, *Small Methods* **2023**, *7*, 2300544.

[2] a) S. Zhou, H. Jang, Q. Qin, L. Hou, M. G. Kim, S. Liu, X. Liu, J. Cho, *Angew. Chem., Int. Ed.* **2022**, *61*, 202212196; b) J. Wang, H. Yang, F. Li, L. Li, J. Wu, S. Liu, T. Cheng, Y. Xu, Q. Shao, X. Huang, *Sci. Adv.* **2022**, *8*, eabl9271; c) L. Yang, H. Ren, Q. Liang, K. N. Dinh, R. Dangol, Q. Yan, *Small* **2020**, *16*, 1906766.

[3] a) K. Jiang, B. Liu, M. Luo, S. Ning, M. Peng, Y. Zhao, Y. R. Lu, T. S. Chan, F. M. de Groot, Y. Tan, *Nat. Commun.* **2019**, *10*, 1743; b) H. Zhang, T. Wei, Y. Qiu, S. Zhang, Q. Liu, G. Hu, J. Luo, X. Liu, *Small* **2023**, *19*, 2207249; c) D. Wu, K. Kusada, Y. Nanba, M. Koyama, T. Yamamoto, T. Toriyama, S. Matsumura, O. Seo, I. Gueye, J. Kim, *J. Am. Chem. Soc.* **2022**, *144*, 3365.

[4] a) J. Yu, Q. He, G. Yang, W. Zhou, Z. Shao, M. Ni, *ACS Catal.* **2019**, *9*, 9973; b) H. Chen, X. Ai, W. Liu, Z. Xie, W. Feng, W. Chen, X. Zou, *Angew. Chem., Int. Ed.* **2019**, *131*, 11531.
[5] T. Chao, W. Xie, Y. Hu, G. Yu, T. Zhao, C. Chen, Z. Zhang, X. Hong, H. Jin, D. Wang, *Energy Environ. Sci.* **2024**, *17*, 1397.
[6] a) K. Wang, J. Zhou, M. Sun, F. Lin, B. Huang, F. Lv, L. Zeng, Q. Zhang, L. Gu, M. Luo, *Adv. Mater.* **2023**, *35*, 2300980; b) Z. Pu, I. S. Amiinu, Z. Kou, W. Li, S. Mu, *Angew. Chem., Int. Ed.* **2017**, *56*, 11559; c) D. Chen, R. Lu, Y. Yao, D. Wu, H. Zhao, R. Yu, Z. Pu, P. Wang, J. Zhu, J. Yu, *J. Mater. Chem. A* **2022**, *10*, 7637; d) K. Huang, C. Lin, G. Yu, P. Du, X. Xie, X. He, Z. Zheng, N. Sun, H. Tang, X. Li, *Adv. Funct. Mater.* **2023**, *33*, 2211102; e) P. Du, C. Lin, X. He, Z. Zheng, X. Xie, K. Huang, M. Lei, H. Tang, *Adv. Compos. Hybrid Mater.* **2023**, *6*, 40.
[7] S. Chen, S. Zhang, L. Guo, L. Pan, C. Shi, X. Zhang, Z. F. Huang, G. Yang, J. J. Zou, *Nat. Commun.* **2023**, *14*, 4127.
[8] a) G. Zhang, G. Wang, Y. Liu, H. Liu, J. Qu, J. Li, *J. Am. Chem. Soc.* **2016**, *138*, 14686; b) Y. Liu, X. Li, S. Zhang, Z. Wang, Q. Wang, Y. He, W. H. Huang, Q. Sun, X. Zhong, J. Hu, *Adv. Mater.* **2023**, *35*, 2300945; c) B. Zhang, Y. Chen, J. Wang, H. Pan, W. Sun, *Adv. Funct. Mater.* **2022**, *32*, 2202227.
[9] a) C. X. Zhao, J. N. Liu, J. Wang, D. Ren, B. Q. Li, Q. Zhang, *Chem. Soc. Rev.* **2021**, *50*, 7745; b) X. Xie, L. Du, L. Yan, S. Park, Y. Qiu, J. Sokolowski, W. Wang, Y. Shao, *Adv. Funct. Mater.* **2022**, *32*, 2110036; c) J. Shan, T. Ling, K. Davey, Y. Zheng, S. Z. Qiao, *Adv. Mater.* **2019**, *31*, 1900510.
[10] a) L. Deng, S. F. Hung, Z. Y. Lin, Y. Zhang, C. Zhang, Y. Hao, S. Liu, C. H. Kuo, H. Y. Chen, J. Peng, *Adv. Mater.* **2023**, *35*, 2305939; b) L. An, C. Wei, M. Lu, H. Liu, Y. Chen, G. G. Scherer, A. C. Fisher, P. Xi, Z. J. Xu, C. H. Yan, *Adv. Mater.* **2021**, *33*, 2006328.
[11] a) H. Yan, Z. Jiang, B. Deng, Y. Wang, Z. J. Jiang, *Adv. Energy Mater.* **2023**, *13*, 2300152; b) Y. Li, W. Wang, M. Cheng, Y. Feng, X. Han, Q. Qian, Y. Zhu, G. Zhang, *Adv. Mater.* **2023**, *35*, 2206351.
[12] a) Z. Chen, L. Guo, L. Pan, T. Yan, Z. He, Y. Li, C. Shi, Z. F. Huang, X. Zhang, J. J. Zou, *Adv. Energy Mater.* **2022**, *12*, 2103670; b) C. Lin, J. L. Li, X. Li, S. Yang, W. Luo, Y. Zhang, S. H. Kim, D. H. Kim, S. S. Shinde, Y. F. Li, *Nat. Catal.* **2021**, *4*, 1012.
[13] a) K. Xiao, Y. Wang, P. Wu, L. Hou, Z. Q. Liu, *Angew. Chem., Int. Ed.* **2023**, *135*, 202301408; b) Z. Shi, Y. Wang, J. Li, X. Wang, Y. Wang, Y. Li, W. Xu, Z. Jiang, C. Liu, W. Xing, *Joule* **2021**, *5*, 2164; c) A. Grimaud, O. Diaz-Morales, B. Han, W. T. Hong, Y. L. Lee, L. Giordano, K. A. Stoerzinger, M. T. Koper, Y. Shao-Horn, *Nat. Chem.* **2017**, *9*, 457.
[14] a) Y. Wang, X. Lei, B. Zhang, B. Bai, P. Das, T. Azam, J. Xiao, Z. S. Wu, *Angew. Chem., Int. Ed.* **2024**, *63*, 202316903; b) J. Wang, C. Cheng, Q. Yuan, H. Yang, F. Meng, Q. Zhang, L. Gu, J. Cao, L. Li, S. C. Haw, *Chem* **2022**, *8*, 1673.
[15] W. Zhai, Y. Chen, Y. Liu, T. Sakthivel, Y. Ma, Y. Qin, Y. Qu, Z. Dai, *ACS Nano* **2023**, *17*, 17254.
[16] a) S. Zhao, Y. Liu, Y. Chen, L. Li, W. Zhai, Z. Guo, Z. Dai, *J. Mater. Chem. A* **2024**, *12*, 10704 b) L. Deng, F. Hu, M. Ma, S. C. Huang, Y. Xiong, H. Y. Chen, L. Li, S. Peng, *Angew. Chem., Int. Ed.* **2021**, *60*, 22276.
[17] C. Xia, L. Huang, D. Yan, A. I. Douka, W. Guo, K. Qi, B. Y. Xia, *Adv. Funct. Mater.* **2021**, *31*, 2105021.
[18] S. Xin, Y. Tang, B. Jia, Z. Zhang, C. Li, R. Bao, C. Li, J. Yi, J. Wang, T. Ma, *Adv. Funct. Mater.* **2023**, *33*, 2305243.
[19] T. Li, S. Li, Q. Liu, J. Yin, D. Sun, M. Zhang, L. Xu, Y. Tang, Y. Zhang, *Adv. Sci.* **2020**, *7*, 1902371.
[20] Y. Wang, R. Yang, Y. Ding, B. Zhang, H. Li, B. Bai, M. Li, Y. Cui, J. Xiao, Z. S. Wu, *Nat. Commun.* **2023**, *14*, 1412;
[21] C. Hu, K. Yue, J. Han, X. Liu, L. Liu, Q. Liu, Q. Kong, C. W. Pao, Z. Hu, K. Suenaga, *Sci. Adv.* **2023**, *9*, 9144.
[22] Y. Zhao, H. Cong, P. Li, D. Wu, S. Chen, W. Luo, *Angew. Chem., Int. Ed.* **2021**, *133*, 7089.
[23] Y. Liu, L. Li, L. Wang, N. Li, X. Zhao, Y. Chen, T. Sakthivel, Z. Dai, *Nat. Commun.* **2024**, *15*, 2851.
[24] Q. M. Luo, Y. W. Zhao, L. Sun, C. Wang, H. Q. Xin, J. X. Song, D. Y. Li, F. Ma, *Chem. Eng. J.* **2022**, *437*, 135376.
[25] S. C. Sun, H. Jiang, Z. Y. Chen, Q. Chen, M. Y. Ma, L. Zhen, B. Song, C. Y. Xu, *Angew. Chem., Int. Ed.* **2022**, *61*, 202202519.
[26] a) W. Zhai, Y. Chen, Y. Liu, Y. Ma, P. Vijayakumar, Y. Qin, Y. Qu, Z. Dai, *Nano-Micro Lett.* **2024**, *16*, 115; b) Y. Luo, P. Wang, G. Zhang, S. Wu, Z. Chen, H. Ranganathan, S. Sun, Z. Shi, *Chem. Eng. J.* **2023**, *454*, 140061.
[27] W. Yan, H. Ma, X. Zhao, Y. Zhang, P. Vishniakov, X. Wang, X. Zhong, Z. Hong, M. Y. Maximov, L. Song, *Small* **2023**, *19*, 2208270.
[28] a) H. Yu, M. Hu, C. Chen, C. Hu, Q. Li, F. Hu, S. Peng, J. Ma, *Angew. Chem., Int. Ed.* **2023**, *62*, 202314569; b) Y. Chen, Y. Liu, L. Li, T. Sakthivel, Z. Guo, Z. Dai, *Adv. Funct. Mater.* **2024**, *34*, 2401452; c) P. Chen, X. Su, C. Wang, G. Zhang, T. Zhang, G. Xu, L. Chen, *Angew. Chem., Int. Ed.* **2023**, *135*, 202306224.
[29] a) C. Rong, X. Shen, Y. Wang, L. Thomsen, T. Zhao, Y. Li, X. Lu, R. Amal, C. Zhao, *Adv. Mater.* **2022**, *34*, 2110103. b) J. Yang, Y. Shen, Y. Sun, J. Xian, Y. Long, G. Li, *Angew. Chem., Int. Ed.* **2023**, *135*, 202302220.
[30] L. Zhang, J. Zhang, H. Yu, J. Yu, *Adv. Mater.* **2022**, *34*, 2107668.
[31] a) D. Chen, R. Lu, R. Yu, Y. Dai, H. Zhao, D. Wu, P. Wang, J. Zhu, Z. Pu, L. Chen, *Angew. Chem., Int. Ed.* **2022**, *61*, 202208642; b) L. Hou, Z. Li, H. Jang, Y. Wang, X. Cui, X. Gu, M. G. Kim, L. Feng, S. Liu, X. Liu, *Adv. Energy Mater.* **2023**, *13*, 2300177.
[32] H. Xin, L. Sun, Y. Zhao, Q. Luo, S. Guo, D. Li, Y. Chen, N. Ogiwara, H. Kitagawa, *Appl Catal B* **2023**, *330*, 122645.
[33] a) Y. Xu, Z. Mao, J. Zhang, J. Ji, Y. Zou, M. Dong, B. Fu, M. Hu, K. Zhang, Z. Chen, S. Chen, H. Yin, P. Liu, H. Zhao, *Angew. Chem., Int. Ed.* **2024**, *136*, 202316029; b) Y. Wen, P. Chen, L. Wang, S. Li, Z. Wang, J. Abed, X. Mao, Y. Min, C. T. Dinh, P. D. Luna, R. Huang, L. Zhang, L. Wang, L. Wang, R. J. Nielsen, H. Li, T. Zhuang, C. Ke, O. Voznyy, Y. Hu, Y. Li, W. A. Goddard Iii, B. Zhang, H. Peng, E. H. Sargent, *J. Am. Chem. Soc.* **2021**, *143*, 6482.
[34] a) R. Liu, M. Sun, X. Liu, Z. Lv, X. Yu, J. Wang, Y. Liu, L. Li, X. Feng, W. Yang, *Angew. Chem., Int. Ed.* **2023**, *135*, 202312644; b) D. Feng, P. Wang, R. Qin, W. Shi, L. Gong, J. Zhu, Q. Ma, L. Chen, J. Yu, S. Liu, *Adv. Sci.* **2023**, *10*, 2300342.
[35] Z. W. Seh, J. Kibsgaard, C. F. Dickens, I. Chorkendorff, J. K. Nørskov, T. F. Jaramillo, *Science* **2017**, *355*, 4998.
[36] Y. Pan, X. Xu, Y. Zhong, L. Ge, Y. Chen, J.-P. M. Veder, D. Guan, R. O'Hayre, M. Li, G. Wang, *Nat. Commun.* **2020**, *11*, 2002,.
[37] R. Chen, Z. Wang, S. Chen, W. Wu, Y. Zhu, J. Zhong, N. Cheng, *ACS Energy Lett.* **2023**, *8*, 3504.
[38] X. Chen, Q. Wang, Y. Cheng, H. Xing, J. Li, X. Zhu, L. Ma, Y. Li, D. Liu, *Adv. Funct. Mater.* **2022**, *32*, 2112674.